Dislocations interacting with a pore in an elastically anisotropic single crystal nickel-base superalloy during hot isostatic pressing

Antoine Ruffini, Yann Le Bouar, Alphonse Finel, Alexander I. Epishin, Bernard Fedelich, Titus Feldmann, Bernard Viguier, Dominique Poquillon

Dislocations interacting with a pore in an elastically anisotropic single crystal nickel-base superalloy during hot isostatic pressing

A. Ruffini[a,*], Y. Le Bouar[a], A. Finel[a], A. I. Epishin[c], B. Fedelich[d], T. Feldmann[d], B. Viguier[e], D. Poquillon[e]

[a] *Université Paris-Saclay, ONERA, CNRS, Laboratoire d'étude des microstructures, 92322, Châtillon, France.*
[b] *Technical University of Berlin, Berlin, Germany*
[c] *Merzhanov Institute of Structural Macrokinetics and Materials Science, Chernogolovka, Russia*
[d] *Federal Institute for Materials Research and Testing, Berlin, Germany*
[e] *CIRIMAT, CNRS – University of Toulouse, Toulouse, France*

Abstract

The formation of pores in CMSX-4 nickel based superalloys is detrimental to the service life of the material. A way to avoid the problem is to treat the superalloys under Hot Isostatic Pressing (HIP), which enables a large volume fraction of pores to be annihilated. This paper aims to understand the contribution of plastic activity related to the gliding of dislocations on the pore annihilation. Simulations based on a phase-field model of dislocation are performed and make it possible to consider the strong anisotropy of the CMSX-4 under HIP conditions in conjunction to the strong elastic heterogeneity introduced by the pore. For pores with a radius of few micrometers, it is shown that edge parts of dislocation lines that present an extra half atomic plane oriented towards the pore are stacked above and under it in the direction which is perpendicular to their slip-planes, causing an increase of the number of dislocation along the four octahedral directions of the FCC single crystal which intersect the pore center. Results are streamlined within the isotropic elastic theory of dislocations. Effects of elastic anisotropy and dislocation reactions are also investigated in order

*Corresponding author
Email address: antoine.ruffini@onera.fr (A. Ruffini)

to specify what would be the dislocation configuration around a pore in CMSX-4 under HIP conditions. Notably, the elastic anisotropy is shown to significantly modify the arrangement of dislocations close to the pore equator. Simulations also allow for the characterization of pore/dislocation interactions when dislocations are involved in Low Angle Boundaries as experimentally observed.
Keywords: HIP, Superalloys, Dislocation, Pore, Voids, Phase-field

1. Introduction

The CMSX-4 is a single crystal nickel based superalloy used in aeronautics to cast turbine blades [1, 2]. After solidification and homogenization treatments, many pores are formed and act as nucleation sites for micro-cracks, ultimately causing the material to fail [3, 4].

The solidification pores are created during dendritic growth of single crystals [5]. They are quite large, up to a maximum diameter of 100 μm, and have irregular shapes [6]. Usually, they appear in Low Angle Boundaries (LABs) separating adjoined dendrites disorientated by about 1 to 2°. The homogenization pores are formed during the subsequent heat treatments. They are smaller, up to a maximum diameter of about 5-10 μm, and their shape is rather spherical [7]. Generally, as it is shown in Fig. 1, they are located in interdendritic LABs as well as in intradentritic LABs between mosaic blocks disorientated by about 0.1° or less.

In the present context, after its elaboration, the CMSX-4 is treated by Hot Isostatic Pressing (HIP), at a pressure of 103 MPa and temperature of 1288°C, which is close to the melting point. This procedure removes a large number of pores, which results in a significant increase in the material life span [8].

At this temperature, the CMSX-4 is constituted of a single γ phase in which several mechanisms are assumed for contributing to pore closure: dislocation glide [9], dislocation climb, vacancy diffusion [10]... These mechanisms are coupled and occur at different space and time scales which makes an exhaustive description of pore annihilation very difficult. As a consequence, pore closure

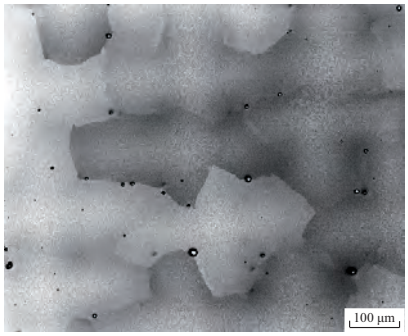

Figure 1: Pores in heat-treated single crystal of nickel-base superalloy CMSX-4. Cross section of dendrite with (001) plane, contrasted in back-scattered electrons (BSE) in a scanning electron microscope (SEM).

kinematics are experimentally quantified without a real insight on the control parameters and only qualitative assertions are generally provided based on the aforementioned annihilation mechanisms.

To go beyond this, numerical simulations can be performed. For example, in [11], the pore shape and its closure kinematics are investigated using Finite Elements Methods and a crystal plasticity model formulated at finite strain. Such simulations allow for providing some qualitative results but fail to correctly reproduce the pore closure kinetics – which are an order of magnitude higher than the experimental ones – as well as the shape of the closing pore – exhibiting corners not observed in real context. These drawbacks may be related to both the absence of "surface energy" in the pore surface description and the phenomenological model of plasticity that does not account for the heterogeneity of the plastic flow related to transport effects. One of the motivations for this work is to go beyond this.

For that purpose, the contribution of plastic activity related to the gliding of dislocations on the pore annihilation is investigated by using a phase-field approach developed in [12], which allows for the consideration of the plastic transport at the dislocation level. This phase field model, originally developed for studying FCC materials with strong elastic heterogeneities and free surfaces,

is used in the present work to characterize more rigorously pore/dislocations interactions in the context of Ni-base superalloys during HIP, and also to perform simulations extended to more realistic reacting dislocations and specific initial dislocation arrangements reproducing Low Angle Boundaries (LABs). More generally, this work aims to characterize interactions between dislocations and a spherical pore when they are involved in face-centered cubic elastically anisotropic materials under isostatic loading. Another reason for using a phase-field approach in the present context is that it allows us to describe plastic activity by naturally considering the strong anisotropy of the CMSX-4 in conjunction to the strong elastic heterogeneity introduced by the pore.

The paper is organized as follows. First, the interaction between a pore and gliding dislocations belonging to one slip-system will be investigated. Straight edge dislocations and loops are both considered in an isotropic material and in the anisotropic CMSX-4 crystal. Results will be streamlined within the theory of elasticity. Then, reacting dislocations and a tilt LAB interacting with a pore will be studied in order to identify the arrangement of dislocations gliding around a pore in more realistic contexts. Finally, scenarios of dislocations inducing pore closure will be proposed and discussed with respect to the obtained numerical results.

2. Pore interacting with dislocations that belong to one slip-system

2.1. Straight edge dislocations

The gliding of straight edge dislocations localized close to a pore is investigated by calculating the stress-induced gliding force acting on them. The stress field generated by a pore of radius R_p embedded in an infinite medium under pressure p is derived from the classical theory of elasticity, by assuming that the medium is elastically linear and isotropic [13, 14]. In the spherical coordinates $(O; \overrightarrow{e_r}, \overrightarrow{e_\theta}, \overrightarrow{e_\varphi})$ with pore center as origin, it is found that the resulting stress tensor $\overline{\overline{\sigma}}$ can be partitioned as $\overline{\overline{\sigma}} = \overline{\overline{\sigma}}_r + \overline{\overline{\sigma}}_{hydro}$ where $\overline{\overline{\sigma}}_r$ is a purely radial

tensor given by:

$$\overline{\overline{\sigma}}_r = \sigma \begin{pmatrix} 1 & 0 & 0 \\ 0 & 0 & 0 \\ 0 & 0 & 0 \end{pmatrix}_{r,\theta,\varphi} \quad \text{with} \quad \sigma = \frac{3}{2} p \left(\frac{R_p}{r} \right)^3, \tag{1}$$

and $\overline{\overline{\sigma}}_{hydro}$ a purely hydrostatic tensor given by:

$$\overline{\overline{\sigma}}_{hydro} = \sigma_{\theta\theta} \begin{pmatrix} 1 & 0 & 0 \\ 0 & 1 & 0 \\ 0 & 0 & 1 \end{pmatrix}_{r,\theta,\varphi} \quad \text{with} \quad \sigma_{\theta\theta} = -p \left(1 + \frac{1}{2} \left(\frac{R_p}{r} \right)^3 \right). \tag{2}$$

For gliding dislocations, hydrostatic stresses do not contribute to the Peach-Koehler force. Locally, the present problem is thus very similar to that of a uniaxial tensile test along $\overrightarrow{e_r}$ under stress σ for which the gliding force per unit line length is known to be [15]:

$$\overrightarrow{F}_g = \tau \; b \; \overrightarrow{n} \times \overrightarrow{\xi}. \tag{3}$$

In this relationship, $\overrightarrow{b}$ (or the norm b) is the Burgers vector of dislocation, $\overrightarrow{n}$ the unit vector perpendicular to its slip-plane and $\overrightarrow{\xi}$ the unit vector tangent to its line direction. The important term is the *resolved shear stress* τ given by:

$$\tau = \overrightarrow{n} \cdot \overline{\overline{\sigma}} \cdot \frac{\overrightarrow{b}}{b} = m \; \sigma, \tag{4}$$

which quantifies the glide force on a dislocation in its slip-plane according to the Schmid factor $m = \cos\alpha \cos\beta$ defined with α as the angle between $\overrightarrow{b}$ and $\overrightarrow{e_r}$, and β as the angle between $\overrightarrow{n}$ and $\overrightarrow{e_r}$. This relationship shows that the glide force on a dislocation is proportional to σ (that is rapidly decreasing with r) and also that, for a given σ, gliding is promoted when m is maximized (that it when $\alpha = \beta = 45°$ similarly to a uniaxial load).

By applying the previous formulas, the gliding force induced by the stress field generated by the pore under pressure is finally found to be:

$$\overrightarrow{F}_g = \frac{3}{2} p b \left(\frac{R_p}{r} \right)^3 m \; \overrightarrow{n} \times \overrightarrow{\xi}. \tag{5}$$

In what follows, we consider the face-centered cubic (FCC) dislocation slip-systems that correspond to the crystallography of the CMSX-4 single crystal under HIP conditions. To be more specific, let us assume straight edge dislocations parallel to $\overrightarrow{e_z}$ characterized by $\overrightarrow{b} = a_0/2[110]$ (a_0 is the FCC lattice parameter) and $\overrightarrow{n} = [1\bar{1}1]/\sqrt{3}$ in the $(0; \overrightarrow{e_x}, \overrightarrow{e_y})$ basis defined by $\overrightarrow{e_x} = \overrightarrow{b}/b$ and $\overrightarrow{e_y} = \overrightarrow{n}$. In this basis, the resolve shear stress corresponding to this slip-system is:

$$\tau(x, y) = \frac{3}{2} p R_p^3 \frac{xy}{(x^2 + y^2)^{\frac{5}{2}}}, \tag{6}$$

such as plotted in Fig. 2.

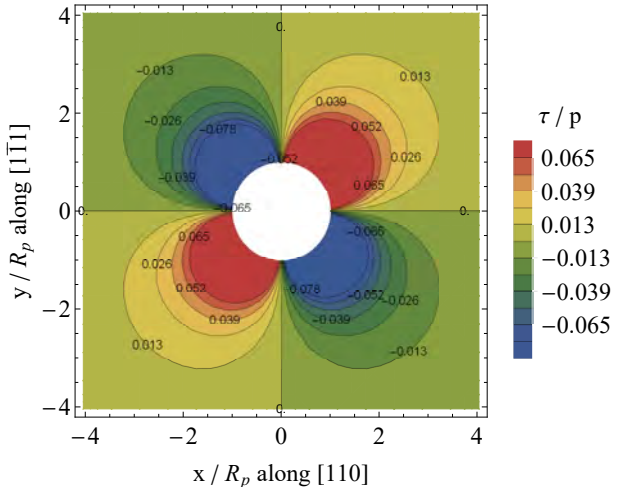

Figure 2: Normalized resolved shear stress τ/p in the $(0; \overrightarrow{e_x}, \overrightarrow{e_y})$ basis defined by $\overrightarrow{e_x} = \overrightarrow{b}/b$ and $\overrightarrow{e_y} = \overrightarrow{n}$.

In this basis, $\overrightarrow{n} \times \overrightarrow{\xi} = -\overrightarrow{e_x}$ and sign of the force is opposed to that of the resolved shear stress (and ultimately the Schmid factor m). In Fig. 2, τ passes from negative to positive values when the slip-plane is above the equatorial plane of the pore ($y > 0$) indicating that there is a stable equilibrium position for this type of dislocation, above the pore, along the (Oy) axis. On the contrary, resolved shear stress passes from positive to negative values under the equatorial plane of the pore ($y < 0$) which indicates that there is an unstable equilibrium position under the pore for this type of dislocation.

This situation is highlighted in Fig. 3 where three distinct regions are identified. Region ① is related to $y > R_p$, where dislocations are dragged from their initial position to the (Oy) axis and where they adopt an equilibrium stacking configuration. Region ② is related to $0 < y < R_p$, where dislocations reach the pore and contribute to a transport of matter over the intersected pore surface. Region ③ is related to $y < 0$, where dislocations are repelled to infinity by the pore-induced stress field.

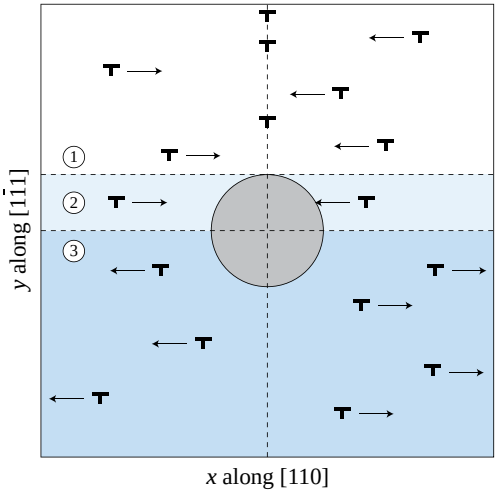

Figure 3: Highlight on regions ①, ② and ③ around the pore (in gray) related to the three expected behaviors discussed in the text about dislocations ($\top$) belonging to slip-system $\overrightarrow{b} = a_0/2[110]$ and $\overrightarrow{n} = [1\bar{1}1]/\sqrt{3}$ in the $(0; \overrightarrow{e_x}, \overrightarrow{e_y})$ basis defined by $\overrightarrow{e_x} = \overrightarrow{b}/b$ and $\overrightarrow{e_y} = \overrightarrow{n}$.

Since the resolved shear stress decreases with the cube of r, it is not expected to observe a significant effect on the movement of dislocations localized far from the pore (typically, on the radial direction $\theta = 45°$ that maximizes the Schmid factor, τ drops below $p/1000$ when $r \approx 10\ R_p$). Moreover, since the resolved shear stress is proportional to the Schmid factor, it cancels out in the equatorial plane of the pore ($y = 0$) indicating that the movement of a straight edge dislocation is not affected by the presence of a pore when its slip-plane intersects the pore center. It is worth mentioning that the image force of the dislocation (due to the pore surface) is not considered here and may invalidate

this conclusion for parts of the line localized close to the pore.

Now, if we consider a dislocation ($\perp$) presenting an extra half plane oriented towards $\overrightarrow{e_y}$, a similar conclusion can be formulated but the stable position for that type of dislocation is under the pore and not above it as in the other case. Ultimately, this should lead us to a configuration shown in Fig. 4 in which "plane to pore" straight edge dislocations (presenting an extra half plane oriented towards the pore) have a stable position under and above the pore along the (Oy) axis while the "plane from pore" straight edge dislocations (presenting an extra half plane oriented from the pore) are repelled.

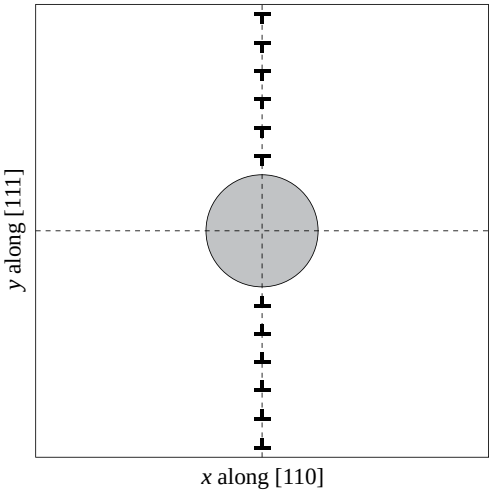

Figure 4: Final expected equilibrium arrangement of dislocations ($\top$) and ($\perp$) around the pore (in gray) by considering slip-system $\overrightarrow{b} = a_0/2[110]$ and $\overrightarrow{n} = [1\bar{1}1]/\sqrt{3}$ in the $(0; \overrightarrow{e_x}, \overrightarrow{e_y})$ basis defined by $\overrightarrow{e_x} = \overrightarrow{b}/b$ and $\overrightarrow{e_y} = \overrightarrow{n}$.

In summary, if a pore already exists in a given system, "plane to pore" straight edge dislocations gliding into different slip-planes should stack under and above the pore in a direction corresponding to the normal of their slip-planes. Conversely, if dislocations already exist and adopt the arrangement exposed in Fig. 4, they would form a tilt Low Angle Boundary (LAB) such as described by a simple Read and Shockley model [16] which may favor the formation of a pore at locations where LABs are joined and where the stable

configuration exposed in Fig. 4 turns out to be recovered. In both cases, this is the stable arrangement of straight edge dislocations that must be expected in the vicinity of a pore.

To go beyond this 2D-like analysis, 3D dislocation dynamics simulations are needed. This will enable us to address the question of more realistic 3D dislocation configurations (curvature effects) and to include the effect of elastic anisotropy, the elastic interactions between dislocations and the image force induced by pore surface. To do this, a phase-field model of dislocations (PFMD) that we have recently developed and which is exposed in detail in [12] is considered. This model is briefly recalled in Appendix A.

2.2. Dislocation loops

The PFMD is now used to numerically investigate arrangements of dislocation loops in the vicinity of a pore. We consider the situation represented in Fig. 5 with slip-system $\overrightarrow{b} = a_0/2[110]$ and $\overrightarrow{n} = [1\bar{1}1]/\sqrt{3}$ which corresponds to $s = 1$ in Tab. A.2.

In these simulations, a cubic system of $(100d)^3$ FCC voxels is considered with a pore of radius $R_p = 15d$ at its center (spherical cavity in which the elastic coefficients are fixed at zero). The physical distance between two cubic numerical nodes is set at $d = 672.53a_0 = 247.63$ nm leading to a pore radius of $R_p = 3.71$ μm and a total cubic system size of 24.76 μm side [1]. In a first simulation, a elastically isotropic material is considered that can easily be compared to the system of subsection 2.1. In a second simulation, the elastically anisotropic CMSX-4 under HIP conditions is investigated using the data exposed in Fig. 1

In the isotropic system, the bulk modulus $K = 169.93$ GPa is that of the CMSX-4, while an effective shear modulus $\mu = \sqrt{C'\ C_{44}} = 32.32$ GPa is considered. This shear modulus corresponds to that of the Scattergood and Bacon approximation [18], which allows for reproducing the effective FCC anisotropic

[1] The choice of these values is arbitrary but consistent with the experimental data. It is due to technical and numerical operating conveniences.

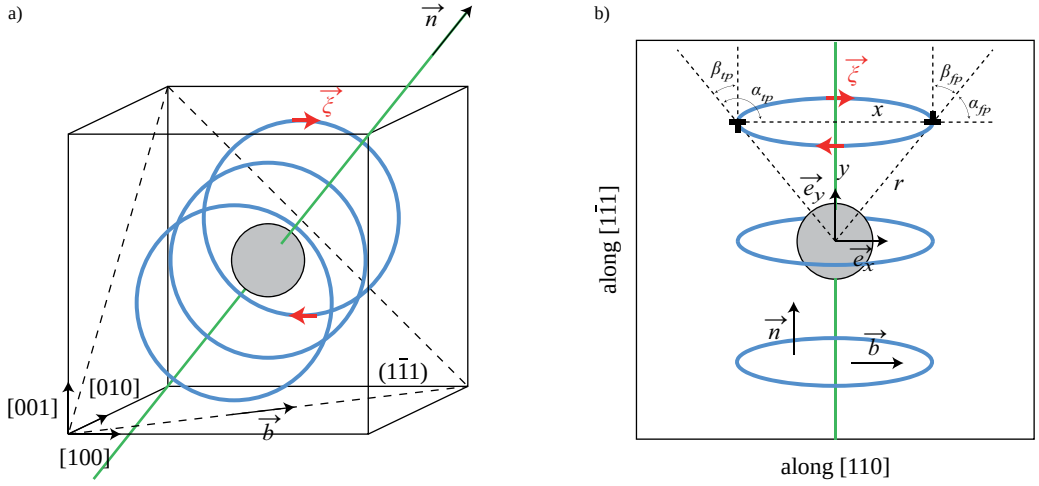

Figure 5: (a) Dislocations loops (in blue) around a pore (in gray) corresponding to the slip system $\overrightarrow{b} = a_0/2[110]$ and $\overrightarrow{n} = [1\bar{1}1]/\sqrt{3}$ (green axis). Tangent vectors $\overrightarrow{\xi}$ (in red) indicate line orientation of the loops. (b) Side view of the loops in the $(0; \overrightarrow{e_x}, \overrightarrow{e_y})$ basis defined by $\overrightarrow{e_x} = \overrightarrow{b}/b$ and $\overrightarrow{e_y} = \overrightarrow{n}$ like in subsection 2.1. Angles α and β involved in the Schmid factor (see Eq. (4)) are represented with subscripts *tp* and *fp* for the "plane to pore" and "plane from pore" edge components respectively. (See colors on-line)

behavior of dislocations in an effective elastically isotropic medium (see details in Appendix B.2 of [19]). In that respect, the {111} shear modulus $\mu_{111} = (2C' + C_{44})/3 = 33.17$ GPa (quantifying the shear stress response to a shear strain acting on a {111} plane) could also have been used as it is here coincidentally very close to μ. Periodic boundary conditions (PBCs) are systematically considered.

The initial condition considered in both simulations is shown in Fig. 6a. This corresponds to the annotated simplified scheme presented in Fig. 5. It consists of five dislocation loops per periodic cell with a radius of $R = 45d = 11.14$ μm from slip-system $s = 1$, initially stacked and centered along the $[1\bar{1}1]$ axis which intersects the pore center.

The final configuration corresponding to the isotropic system is presented in Fig. 6b. It is found that the "plane to pore" edge parts of a loop are dragged along the $\overrightarrow{b}$ direction [110] from their initial position to a location of their slip-

CMSX-4 (HIP) param.	$a_0 = 0.368$ nm
Burgers vector	$b = a_0/\sqrt{2} = 0.260$ nm
Pore radius	$R_p = 3.71\ \mu m$
Pressure (HIP)	$p = 103$ MPa
Temperature (HIP)	$T = 1288°$C
Bulk modulus	$K = 164.93$ GPa
Shear moduli	$C' = 15.05$ GPa
	$C_{44} = 69.40$ GPa
Zener anisotropy ratio	$A = C_{44}/C' = 4.61$

Table 1: CMSX-4 data under HIP conditions [17]

plane which is the closest to the pore surface. This results in the stacking of the "plane to pore" edge components under and above the pore along the $[1\bar{1}1]$ cubic direction which corresponds to the normal $\overrightarrow{n}$ of their slip-plane. Conversely, the "plane from pore" parts of the loops are observed to move away from the pore until a circular shape is finally adopted. When loops are far from the pore, they are seen to collapse as well as the equatorial loop that vanishes in the final stage.

Similar qualitative observations can be asserted in the CMSX-4 simulation shown in Fig. 6c. What differs from the isotropic case is that the loops adopt a "peanut" shape much less symmetrical than in the isotropic case. Another important difference is that the equatorial loop finally stays in the system and forms two smaller loops with lines that intersect pore surface at its equator, at two locations where purely edge and screw character are identified. This generates two surface steps on the pore equator.

In both simulations, the behavior of the "plane to pore" parts of the loop is comparable to that of the straight edge dislocations studied in 2.1: under the stress field induced by the pore in the system under pressure, a force is generated on the dislocation lines that brings the "plane to pore" edge parts of the loops

to a point of their slip-plane which the closest to the pore surface (the point passing through normal $\overrightarrow{n}_1 = [1\bar{1}1]/\sqrt{3}$ intersecting the pore center). However, the behavior of the "plane from pore" parts of the loops is different since they are observed to be placed at an equilibrium finite distance of the pore instead of being repelled far from it.

This difference of behavior is actually due to the *line-tension* of loops that tends a curved dislocation to become straight under its own stress field, or here a dislocation loop to collapse. It is a curvature effect. On the contrary to what happens with straight edge dislocations, the repelling force on the "plane from pore" parts of the loop can now be compensated by the force induced by line-tension. This results in equilibrium loop shapes that emerge from this competition.

The line tension can be estimated with the formula:

$$\overrightarrow{F}_{LT} = \frac{-\mu b^2}{4\pi D}\frac{2-\nu}{1-\nu}\left(\ln\left(\frac{2D}{r_0}\right) - 1\right)\overrightarrow{n} \times \overrightarrow{\xi}, \tag{7}$$

that gives the corresponding force per unit length on a dislocation line element [15, 20, 21]. In this case, the loop is assumed to be circular with diameter D, the medium homogeneous and elastically isotropic with shear modulus $\mu = 32.32$ GPa and Poisson ratio $\nu = 0.41$ [2], while $r_0 << D$ is the size of the dislocation core taken to be $r_0 = 2a_0 = 0.736$ nm (see Tab. 1).

For loop diameters D of size comparable to the pore radius R_p, the line-tension related stress amplitude $\sigma_{LT} = \left|\overrightarrow{F}_{LT}\right|/b$ is about 4 MPa. In both simulations, it is thus assumed that loops experience a more-or-less constant average value of $\sigma_{LT} \approx 4$ MPa. In that respect, the loops are not expected to collapse in regions where the pore-induced resolved shear stress τ is higher than this finite value of line-tension related stress amplitude. The 4 MPa τ-contours have been numerically extracted in Figs. 6d and 6e, for the isotropic and anisotropic CMSX-4 respectively. To do this, the resolved shear stress τ

[2] ν is calculated with the bulk modulus K and the shear modulus μ according to $\nu = (3K - 2\mu)/(2(3K + \mu))$.

given by Eq. (4) has been numerically calculated by considering the involved slip-system $s = 1$ with the elastic and geometrical parameters of the simulations. It is worth mentioning that for the isotropic case where the stress tensor $\overline{\overline{\sigma}}$ is known (see subsection 2.1), Eq. (4) gives the exact analytical solution.

The comparison of Figs. 6b and 6c with Figs. 6d and 6e makes the correlation between the dislocation configurations and the τ-contours very apparent. Both in the isotropic and anisotropic CMSX-4 systems, the line-tension does not change the fact that the "plane to pore" parts of the loops are dragged from their initial position to the point of their slip plane which is the closest to the pore surface. In contrast, the remaining part of the loops tends to be pushed forward towards positions where the resolved shear stress τ is not high enough to compensate the natural tendency of the loop to collapse on itself. As a consequence, the loops adopt equilibrium shapes that strongly depend on the material elastic properties. Notably, in the anisotropic CMSX-4 system exposed in Figs. 6c and 6e, the fact that the equatorial loop does not entirely collapse can be explained by the presence of regions where τ exceeds the line-tension related stress value in the equatorial $(1\bar{1}1)$ slip-plane (see white arrow in Fig. 6e). As for the "peanut" shapes of the other loops, they can be explained by the fact that the τ-contour turns out to be highly asymmetrical in the anisotropic crystals.

Thus, the simulations reveal that the elastic anisotropy significantly modifies the arrangement of dislocations close to the pore equator. They also show that the predominant effects come from the iso-anisotropic stress field generated by the pore and this related to line-tension, and that the other effects coming from the image forces and the extra stress field generated by the dislocations on each other can be neglected. Furthermore, other simulations not shown here have been performed with only one dislocation loop gliding in various tested slip-planes (including that intersecting pore equator) which have shown identical final configurations.

2.3. Influence of the parameters

Since the line-tension effects are correctly captured by the relationship given Eq. (7), this former is used to quantify the influence of the elastic, geometrical and loading parameters on the equilibrium configuration of the loops.

In the $(0;\overrightarrow{e_x},\overrightarrow{e_y})$ basis exposed in Fig. 5b, the equilibrium position of the "plane from pore" edge part of a dislocation loop is the couple of points (x,y) described by the parametric equation $\sigma_{LT}\left(D=x\right)=\tau(x,y)$ in which τ is the resolved shear stress given by Eq. (6). Here, the "plane to pore" edge parts of the dislocation loops are assumed to remain close to the (Oy) axis. In polar coordinate, the equality $\sigma_{LT}\left(D=x\right)=\tau(x,y)$ becomes $(r/R_p)^3 L(x)=\chi\cos\theta\sin\theta$, with the radial distance r, a function $L(x)=[\ln\left(2x/r_0\right)-1](2-\nu)/[6\pi(1-\nu)]$ and the parameter:

$$\chi=\left(\frac{p}{\mu}\right)\left(\frac{R_p}{b}\right). \tag{8}$$

For positions $0.01R_p<x<10R_p$, we have $L(x)=1\pm0.50\approx1$ such that the equilibrium position is finally described by the polar equation:

$$\frac{r}{R_p}\approx\left(\chi\cos\theta\sin\theta\right)^{1/3}. \tag{9}$$

By studying the variation of r with respect to θ, it is found that the maximal equilibrium position of the "plane from pore" edge part of the loop x_{max} is for $\theta=26.6°$ and that the maximal vertical position of a dislocation slip-plane y_{max} is for $\theta=63.4°$ that both give:

$$\frac{x_{max}}{R_p}=\frac{y_{max}}{R_p}=0.66\ \chi^{1/3}. \tag{10}$$

As for the maximal radial position r_{max}, it is for $\theta=45°$ that gives:

$$\frac{r_{max}}{R_p}=\left(\frac{\chi}{2}\right)^{1/3}. \tag{11}$$

These formulas show that the range in which the dislocation loops are localized with respect to R_p varies as $\chi^{1/3}$ which increases when the applied pressure p and/or the pore radius R_p increase at the same order, or when the shear modulus μ decreases (Burgers vector b is considered constant for that type of analysis).

Equilibrium position, y_{max}, r_{max} and x_{max} given by Eqs. (9 – 11) are plotted in Fig. 7 for different values of χ going from 10 to 160. The curve related to the simulations is that for which $\chi = 45.41 \approx 40$. This figure graphically highlights the previous analytical results, showing that when a dislocation loop is placed in slip-planes with y coordinates bigger than y_{max}, the "plane from pore" edge part of the loop experiences a force $\delta F_{LT} > \delta F_g$ that causes the loop to collapse. On the contrary, closer to the pore, one gets $\delta F_{LT} < \delta F_g$ and the collapse of the loop is not permitted. In this case, the maximum loop diameter corresponds to x_{max}.

Ultimately, this leads to the configuration already observed in the isotropic simulation and summarized in Fig. 8 where the "plane to pore" edge components of the loops are stacked under and above the pore like in the case of straight edge dislocations, *but only in a close region where the stress field generated by the pore prevents a loop from collapsing.* Also, loops that would be placed in the equatorial plane of the pore must collapse because of the absence of a pore-induced compensating force in this specific plane. Of course this analysis does not apply to the anisotropic CMSX-4 case which has been observed to provide slightly different results.

The diagram exposed in Fig. 7 also allows us to identify a critical pore radius R_p^{crit} under which the resolved shear stress is not able to compensate the stress related line-tension. This is when $r_{max}/R_p = 1$ for which Eq. (11) gives:

$$R_p^{crit} \approx 2 \left(\frac{\mu}{p} \right) b. \tag{12}$$

With the current parameters, *the arrangement of dislocation loops as it is shown in Fig. 8 is not expected for small pores with a radius lower than* $R_p^{crit} \approx 160$ *nm.* In general, Eq. (12) shows that R_p^{crit} linearly decreases with the decrease of shear modulus μ and the increase of applied pressure p.

In the next section, dislocation dynamics simulations are performed to go beyond these results that only involve one slip-system. Notably, one would want to know if the dislocation reactions or some specific initial configurations can change the final arrangement of dislocations such as identified thus far.

3. Pore interacting with reacting dislocations and Low Angles Boundaries

From this section, only the anisotropic CMSX-4 single crystal is investigated as it is the material of interest. Of course, the obtained results may qualitatively be particularized to the isotropic case.

3.1. Coplanar slip-systems

In this part, PFMD simulations are carried out with the aim of accessing the dislocation configuration of reacting coplanar dislocations. To do this, the simulated system used in the previous section is reconsidered but with the initial condition exposed in Fig. 9a. It consists of two loops of radius $R = 30d = 7.43\ \mu$m and $R = 45d = 11.14\ \mu$m from slip-systems $s = 1$ and $s = 2$ respectively, introduced in the same $(1\bar{1}1)$ slip-plane placed at 3.43 μm from the pore surface and centered along the $[1\bar{1}1]$ cubic axis. In what follows, the loops are labeled ss1 and ss2 according to the number of their slip-system found in Tab. A.2.

Intermediate and final dislocation configurations obtained in the anisotropic CMSX-4 single crystal under external pressure $p = 103$ MPa are exposed in Figs. 9b and 9c, respectively. In Fig. 9b, it is found that the "plane to pore" edge part of the loop ss1 is dragged from its initial position to the point of its slip-plane which is the closest to the pore surface (the point belonging to the $[1\bar{1}1]$ axis intersecting pore center). At the same time, two other parts of this loop react with loop ss2 to form dislocation lines of type ss3. In Fig. 9c, the original lines ss1 and ss2 continue to merge under a coplanar junction making lines ss3 extend and finally meet in the final equilibrium configuration. In this last state, the "plane from pore" components of loops ss2 and ss3 are both repelled from the pore leading to an equilibrium shape for these loops that is close to the "peanut" shape identified previously with one slip-system. Their "plane to pore" parts are relocated to the $[1\bar{1}1]$ axis intersecting the pore center leading to a final configuration where loops ss2 and ss3 are joined by a straight edge dislocation ss1 at two triple nodes.

The final loop configuration is emphasized in Fig. 10 where the triple node formed and located on the $[1\bar{1}1]$ axis intersecting the pore center coincides with the edge character of all three slip-systems. At this node, the rule of dislocation reactions $-\overrightarrow{b}_3 = \overrightarrow{b}_1 + \overrightarrow{b}_2$ is granted according to the line orientations highlighted in the figure. Topologically speaking, this enables us to get a triple node with emerging lines with edge character at the point which is the closest to the pore surface and which belongs to their common slip-plane. Dislocation lines emerging from this triple node are separated by an angle of 120°. The other triple node differs from the first by presenting a line ss1 with a purely edge character while dislocation lines ss2 and ss3 have a mixed character of 30° (angle between Burgers vector and the dislocation line).

To summarize, when two coplanar slip-systems are involved, it is shown that the coplanar reactions do not change the fact that the "plane to pore" edge components of the loops are relocated to the point of their slip-plane which is the closest to the pore surface, similar to what was shown with only one slip-system. Here, it just turns out that *a triple node with* 120° *emerging lines with edge character is formed which is enabled by the topology of FCC dislocation reactions.* It is worth noticing that the current arrangement has been reproduced several times with other dissimilar initial conditions where two coplanar dislocations from two distinct slip-systems were introduced. This demonstrates that the configuration of Fig. 10 is really robust, confirming furthermore that what happens is essentially driven by the stress field generated by the pore.

3.2. All slip-systems

In this subsection, simulations involving all slip-systems are performed in order to account for non coplanar dislocation reactions. In the initial condition, the previous pore geometry and elastic parameters of CMSX-4 are reconsidered with twenty-four circular dislocation loops of random radii and positions, arbitrary chosen from every slip-systems. Under an external pressure of $p = 103$ MPa, the dislocations evolve and reach the final configuration exposed in Fig. 11a. In what follows, the loops are labeled with the number of their slip-system

(ss1 to ss12) according to Tab. A.2.

At first sight, the tangled dislocation lines exposed in Fig.11a seems to be quite complex. However, a closer look shows that the final dislocation configuration can actually be rationalized with the mechanisms isolated beforehand: (i) positioning of the "plane to pore" parts of dislocations at the point of their slip-plane which is the closest to the pore surface and repelling of the "plane from pore" parts to remote finite positions, (ii) adoption of a peanut shape for the smaller loops, (iii) anchoring of loops at pore equator because of the strong elastic anisotropy and (iv) coplanar reactions forming triple nodes with 120° emerging lines with edge character, placed along the $\langle 111 \rangle$ direction intersecting pore center. What is new is the formation of junctions and locks whose marginal effects are commented further.

Point (i) is highlighted in Fig. 11b involving ss10 and ss11 where the "plane to pore" parts of the dislocations are found to be placed at the point of their slip-plane which is the closest to the pore surface, while the "plane from pore" resting parts are repelled to remote finite positions. Here, because of the PBCs, the "plane from pore" parts of loop ss11 emerge on the other side of the simulated box where they turn out to become attractive "plane to pore" parts, relative to the pore. This causes the loop to be pinned in the system at both its line parts of edge character and so the final dislocation loop shape to be less affected by line-tension effects. Similar configurations with loops ss6 could also have been highlighted but have not been shown for the sake of brevity.

Point (ii) is illustrated in Fig. 11c involving ss2 and ss9. As opposed to the previous case, the loops are smaller causing their shapes to be closer to the "peanut" shape already characterized in subsection 2.2, with the "plane to pore" edge parts of the loops still placed at the points of their relative slip-plane which is the closest to the pore surface. What is noticeable with these loops is that they have reacted to form a glissile junction of type ss7 (pointed out with the letter [g]) which does not seem to affect their global final shape. Here, one has to say that the glissile junctions are not able to glide in the actual formulation of the PFMD. Hence, even though it seems reasonable to assert that it would

not significantly change the shapes and behaviors of dislocations as identified until now, it is a fact that moving glissile junctions would have changed the final loop configuration such as it is observed in Fig. 11c.

Point (iii) is depicted in Fig. 11d involving loops ss8 and ss9. Small loops localized near the pore equator are observed to intersect this former by forming steps on the spherical surface. These specific configurations are directly related to the elastic anisotropy of CMSX-4. Indeed, it was shown previously that in an isotropic system, the force induced by line-tension effects cannot be compensated in the equatorial region by that related to the stress field generated by the pore. It is therefore important to confirm this result with several slip-systems since it is correlated to a displacive-induced transport of matter which seems to be promoted in strongly anisotropic crystals as it is the case for CMSX-4 placed under HIP conditions.

Point (iv) is emphasized in Fig. 12 in which the Burgers vectors and line orientations of loops ss7, ss8 and ss9 are explicitly indicated. Here, contrary to what is shown in Fig. 10, two triple nodes with 120° emerging lines with edge character are created. They are dragged to the position of their slip-plane which is the closest to the pore surface and which turns out to be common for both nodes. Because forming a quadruple coplanar node is not energetically favorable, these nodes do not merge and finally form a junction whose length would has to depend on the slip-plane/pore distance. Notably, it is expected that the junction length decreases with the slip-plane/pore distance as the inclination of the pore for bringing the nodes at the same place becomes higher and higher.

In Figs. 11c and 11d, one can also notice the presence of Lomer and Hirth locks pointed out by letters [L] and [H], respectively. These locks may somehow provoke pinning. However, they do not significantly modify the global dislocation arrangement which mainly remains controlled by the competition between the stress field of the pore and their line-tension. Note that colinear annihilation reactions have not been observed in this simulation, like in two other simulations not shown here that have been performed to confirm the reproducibility of the typical dislocation arrangements.

In the Supplementary Material, other simulations performed with alternative initial conditions consisting in a network of coplanar gliding dislocations have been performed to possibly provoke unexpected mechanisms. They have lead to the formation of triple nodes with 120° emerging lines with edge character already described in Fig. 12. This tends to demonstrate that the final dislocation configurations are quite insensitive to the initial conditions (random distribution, specific network...) confirming that the arrangement of dislocations located close to a pore is mainly controlled by the stress field that it generates in the crystal, in competition with line-tension effects.

In summary, the more complex dislocation arrangement resulting from the presence of all slip-systems can be explained in terms of the simpler isolated mechanisms characterized previously. This demonstrates that *the aforementioned mechanisms are quite insensitive to non coplanar dislocation reactions. As a consequence, the "stacking mechanism" of dislocation edge parts would have to be expected in the four* $\langle 111 \rangle$ *FCC octahedral directions aligned with the pore center when all slip-systems are activated.* This result might open the way to experimental confrontations.

3.3. Tilt Low Angle Boundaries

In single crystal superalloys such as the CMSX-4, pores are formed during solidification or homogenization treatments and are mainly localized in inter-dendritic zones. Furthermore, the low misalignments of dendrites lead to the formation of Low Angle Boundaries (LABs), which can be described by the stacking of dislocations. Hence, regardless of the way pores are created, it is expected that they stand inside (or at least close to) a LAB. In this part, such a typical configuration is investigated using the PFMD simulations.

The previous simulating box is reconsidered with straight edge dislocations stacking in a way that they reproduce a tilt LAB as it would be in the simple Read and Shockley model [16]. In the initial condition exposed in Fig. 13a, the pore is centered in the simulation box and embedded into a LAB built with edge dislocations from the first slip-system, with Burgers vector $\overrightarrow{b_1}$ and line

orientation $\overrightarrow{\xi} = [\bar{1}12]$, separated by a distance $\ell = 0.57$ μm along $[1\bar{1}1]$[3]. This leads to a LAB misorientation of $\theta_{LAB} = b/\ell = 0.026°$. Note that because of the periodic boundary conditions (PBCs), two LABs are considered separating a tilt and an anti-tilt crystal of $100d\sqrt{2}/4 = 8.76$ μm thickness. In Fig. 13, the first LAB is centered and appears to be in one piece while the other appears as two pieces due to the PBCs. In the central LAB, with respect to the figure's point of view, dislocations stacked above the pore present an extra half plane oriented towards the pore while those stacked under present an extra half plane oriented from the pore. This is the opposite in the lateral LAB.

According to subsection 2.1, one should expect that the bottom part of the central LAB (made with "plane from pore" dislocations) be destabilized as opposed to the upper part (made with "plane to pore" dislocations). This is what is shown in Fig. 13. As time increases, more and more "plane from pore" dislocations placed under the LAB are repelled from their initial position. Some of them adopt a partially circular shape while others merge with dislocations of an opposed Burgers vector that belong to the anti-tilt lateral LAB. What is noticeable is that only the "plane from pore" dislocations localized just under the pore are observed to be destabilized and repelled towards direction $-\overrightarrow{b_1}$. Further away, these dislocations remain static like the "plane to pore" dislocations localized above the pore allowing to maintain the initial straight shape of the LAB. Later in the simulation, the two LABs are observed to collapse which is not shown here as it is specific to our initial conditions and not a general mechanism to be highlighted.

The reason why the "plane from pore" dislocations placed under the pore

[3]In our simulation, ℓ must be higher than $d_{111} = d/\sqrt{3}$ for this distance to be numerically resolved (we chose $\ell = 4d_{111}$). It is thus constrained by the numerical grid spacing d. Since this value has been chosen in order to simulate micro-pores with reasonable computational resources, $d = 247.63$ nm and the maximal misorientation angle is $\theta_{LAB}^{max} = b\sqrt{3}/d = 0.104°$. To access higher values, one should select a smaller value for d but at the cost of higher numerical ressources. That said, such low values are consistent with the low misorientations involved in mosaic blocks as written in the introduction.

are not destabilized when they are localized far from the pore is that they are stabilized by the stress field generated by the LAB itself. In an isotropic elastic medium, this effect can be evaluated in the $(0; \overrightarrow{e_x}, \overrightarrow{e_y})$ basis of Fig. 14 defined with $\overrightarrow{e_x} = \overrightarrow{b}/b$ and $\overrightarrow{e_y} = \overrightarrow{n}$, by comparing the resolved shear stress τ given Eq. (6) with the always attractive stress field σ_{LAB} that a dislocation undergoes by escaping from its LAB along $\overrightarrow{e_x}$. This stress is given by the infinite summation of the shear stress of stacking edge dislocations[4] subtracted from that of the escaping dislocation:

$$\sigma_{LAB}(x) = \frac{\mu b}{2\pi\left(1-\nu\right)}\left[x\left(\frac{\pi}{\ell}\right)^2 \operatorname{csch}^2\left(\frac{\pi x}{\ell}\right) - \frac{1}{x}\right]. \tag{13}$$

Equating Eq. (6) and (13) around $x = 0$ (at first order of the Taylor series) provides a critical distance y_c beyond which the destabilizing stress field generated by the pore is not high enough to compensate the stabilizing stress field of the LAB. This critical distance corresponds to the $y-$range in which "plan from pore" dislocations constituting a LAB are not expected to persist. After simplification, it is shown that:

$$\cdot\frac{y_c}{R_p} \approx \left(\frac{p}{\mu}\right)^{1/4}\left(\frac{2b}{R_p}\right)^{1/4}\frac{1}{\left(\theta_{LAB}\right)^{1/2}}, \tag{14}$$

meaning notably that y_c/R_p will increase with the applied pressure p and will decrease with the pore radius R_p at the same order $1/4$. It is worth noticing that y_c/R_p is more sensitive to the LAB geometry since it will decrease with the square root of the LAB misorientation θ_{LAB}.

By using the simulation data from Tab. 1 with $\theta_{LAB} = 0.026°$ and $\mu = 32.32$ GPa, one gets $y_c/R_p \approx 1.2$ meaning that the LAB is destabilized under the pore over a distance ranging with its radius. This is consistent with the simulation results which shows a slightly more extended zone due to the fact that the idealized straight shape of the LAB considered in the calculation is not preserved in the destabilized region. The elastically isotropic formalism may also induce discrepancies.

[4]See Eq. (B.5) in [16] with $\varphi = \pi/2$, $y = 0$ and ℓ instead of D_y.

Ultimately, this leads to the configuration exposed in Fig. 14 where three distinct regions are identified. In region ① corresponding to $y > 0$, dislocations are stabilized on the (Oy) axis by the stress field generated by both pore and LAB. In region ② corresponding to $0 > y > y_c$, "plane from pore" dislocations are destabilized by the stress field generated by the pore. As indicated in Eq. (14), these dislocations are removed over a $y-$range that inversely depends on the square root of θ_{LAB}. In region ③ related to $y_c > y$, the destabilization stress field induced by the pore is compensated by that of the LAB so that dislocations remain static.

When the LAB does not intersect the pore but is placed in its vicinity, like it is the case for the lateral anti-tilt LAB, the presence of the pore is expected to induce a similar effect by repelling some "plane from pore" dislocations from their initial position. This phenomenon is observed in Fig. 13 for some "plane from pore" dislocations which, in this lateral LAB, are localized above the equatorial plane of the pore. Conversely, some "plane to pore" edge dislocations placed under the equatorial plane of the pore are observed to be attracted under its stress field and turn out to be relocated to the point of their slip plane which is the closest to the pore surface.

In this configuration, still in the isotropic elasticity formalism, it is possible to quantify the lateral $x-$range over which the pore can capture some " plane to pore" dislocations from a distant LAB. One have to identify the critical distance x_c from which the maximized value of resolved shear stress τ given Eq. (6) (corresponding to positions for which $y = x$) is equal to the maximum value of σ_{LAB} given Eq. (13) found to be $\approx \mu b/[2\pi\ell(1-\nu)]$ at distance $\delta x = 0.61\ell$ from the LAB. After simplification, one gets:

$$\frac{x_c}{R_p} \approx \left(\frac{p}{\mu}\right)^{1/3} \frac{1}{(\theta_{LAB})^{1/3}}, \tag{15}$$

showing notably that x_c/R_p will increase with the applied pressure p and will decrease with the LAB misorientation θ_{LAB} at the same order $1/3$. Furthermore, this rescaled value x_c/R_p will not depend on the pore radius R_p as opposed to y_c/R_p.

By using the simulation data from Tab. 1 with $\theta_{LAB} = 0.026°$ and $\mu = 32.32$ GPa, one gets $x_c/R_p \approx 1.8$ meaning that a LAB can be destabilized if its distance from the pore center is in the order of magnitude of the pore radius[5]. This result is consistent with the simulation results. It is worth noticing that x_c/R_p inversely varies with the cubic root of θ_{LAB} as opposed to y_c/R_p which exhibits a more sensitive inverse square root dependency.

In summary, *tilt LABs containing a pore are destabilized in a region where the LAB presents "plane from pore" edge dislocations*, over a range which is in the order of magnitude of the pore radius. *When tilt LABs are placed close to a pore, dislocations may be attracted and placed to the point of their slip plane which is the closest to the pore surface* provided that the distance between the LAB and pore is in the order of magnitude of the pore radius.

4. Discussion and conclusion

Pore collapse in Nickel base superalloys under HIP condition is the result of complex processes involving voids, dislocations and LABs. The aim of this work is to contribute to a better understanding of the phenomena involved, in particular dislocation glide.

The contribution of dislocation movement to the change in pore volume has been the subject of several studies, mainly at the atomic scale, in the context of the growth of nanometric pores under severe conditions such as laser shocks. Mechanisms such as dislocation loops nucleation at the void surface, glide of complex emergent dislocation structures, formation of prismatic loops and capture of pre-existing dislocations have been proposed [22, 23, 24, 25, 26, 27, 28, 29, 30, 31, 32]. To finish this paper, we discuss the relevance of these mechanisms for pore closure under HIP, in light of the results achieved in our work, which shows that micrometer scaled pores under hydrostatic pressure are able

[5] Actually, the closest distance without destabilization would have to be $x_c + \delta x$ but this correction is not relevant, as $\ell \ll R_p$ and the other approximations of the calculation might also be pernicious.

to attract dislocations (of which some of them may anchor to the pore surface), with their "plane to pore" edge parts that are likely to be stacked along the four octahedral directions of the FCC single crystal.

First, for typical pressures used in HIP conditions, the nucleation of dislocations from a micrometer pore is a scenario which can be discarded. Indeed, the growth of a dislocation loop nucleus requires that the pore-induced stress amplitude overcomes that related to both the image and line-tension forces. Theoretical estimations [22, 24] show that the required pressure for dislocation loop nucleation decreases with the pore size but remains above several GPas which is at least an order of magnitude higher than the pressure involved during HIP.

Furthermore, in a single crystal superalloy, pores are generally formed in interdendritic regions where LABs are created, implying the existence of dislocations in the pore vicinity. Also, as it is shown in our simulations, when dislocations are initially placed away from the pore, they tend to be attracted and relocated to its vicinity such that the dislocation density increases in its neighborhood. The strong anisotropy of the CMSX-4 may also increases this density around the pore equator since the dislocations cannot entirely be captured in this region (see section 2.2) . It is thus more probable that the pore closure is induced by the trapping of available preexisting dislocations than by their nucleation at its surface. Note that the importance of pre-existing dislocation has also been pointed out by several authors in the context of void growth [33, 34, 30, 32].

We now analyze the pore closure mechanisms expected from the final dislocation configurations identified in our simulations showing that: (i) dislocations may intersect the pore and be captured through its surface, (ii) they may stand close to the pore with their "plane to pore" edge parts aligned along the four octahedral directions.

In case (i) for which dislocations intersect the pore, its closure may be induced by a direct transport of matter through its surface. The most probable scenario would then involve prismatic loops resulting from cross-slip of the screw

parts of some anchored loops [35, 31, 32, 30] as it is illustrated in Fig. 15. The mechanism described here is very close to that of coherency loss of a precipitate by prismatic punching [36] expect that it involves pre-existing dislocations in the pore vicinity. In the present context, the formation of prismatic loops is expected because of the existence of cross-slip forces close to the pore surface [37] and of the very high temperature able to thermally activate this mechanism.

Note that the strong elastic anisotropy on the CMSX-4 superalloy at high homologous temperature impacts the stability of the dislocation loops anchored at the pore surface (see section 2.2). Therefore, including the elastic anisotropy may be of importance for a quantitative estimation of the consequences of prismatic loop formation on pore closure.

In case (i) for which dislocations intersect the pore, other mechanisms may be of importance. Indeed, the multiple slips of a large number of dislocations is also expected to contribute to pore collapse, whether through the formation of specific interacting dislocation configurations whose topology may permit for some crystallographic planes to be extracted from the pore [27] or through local inward surface atomic rearrangements identified in atomistic simulations under such multiple slips [38, 39, 40]. Of course, testing the relevance of such situations for micrometer pores would require to perform additional simulations using mesoscopic approaches including both free surfaces, dislocation glide and cross-slip. This could be reached by discrete dislocation dynamics simulations using local rules for the short-range interactions between dislocations and surfaces [31, 32] or by extending the elastically non-linear model proposed in [36] to the FCC symmetry. Note finally that surface diffusion is also an important ingredient to explain the spherical shape during pore shrinkage, as plastic mass transport is expected to be anisotropic.

In case (ii) for which dislocation glide planes do not intersect the pore, our simulations show that gliding dislocations reach an equilibrium position in the pore vicinity favoring edge type orientations. From these configurations, pore shrinkage may be induced by vacancy diffusion where climbing dislocations act as source/sink of vacancies.

In nickel base single crystal superalloys under HIP, pores are removed in a matter of hours at a high homologous temperature, implying that scenarios involving diffusive mechanisms are realistic.

Indeed, the vacancy diffusion between dislocations acting as vacancy sources/sinks and a spherical pore has been studied using a simplified geometry of LAB [10]. In this paper, it is shown that, provided that the pore size distribution is taken into account, the time evolution of the volume fraction of pores predicted by the model is in reasonable agreement with available experiments.

However, our study of dislocations and LAB in the pore vicinity during HIP suggests that the rapid glide of dislocations leads to dislocation configurations much more complex than the perfect immobile LAB considered in [10]. The presence of these dislocation configurations close to the pore may significantly modify the way vacancy diffusion-induced pore closure occurs by constituting a non trivial distribution of sources and sinks. Because dislocation glide is much faster than climb, this point could be analyzed using a phase field model of dislocation climb [41] starting from the final stacking arrangements observed in our simulations.

A scenario combining dislocation glide and climb is illustrated in Fig. 16. Here, it is worth mentioning that the final stages represented in this figure are more speculative and would deserve to be investigated more rigorously by the consideration of numerical modeling that explicitly couples vacancy diffusion, dislocation climb and pore evolution. Such work is currently under consideration through the development of a phase field approach drawn on [41].

In summary, both theoretical and numerical investigations have been carried out to analyze the dislocation glide and resulting arrangements around a micrometer-sized spherical pore in the CMSX-4 superalloy under HIP conditions. We have used a phase field model of dislocation glide in a FCC crystal that is able to include surfaces, and we have performed 3D simulations to analyze the formation of dislocation arrangements in the vicinity of the pore.

For dislocations whose glide plane does not intersect the pore, it is shown that edge parts of dislocation lines that present an extra half atomic plane

oriented towards the pore are stacked in the direction which is perpendicular to their slip-planes. This results in an increase of the dislocation density along the four octahedral directions of the FCC single crystal which intersect the pore center. This main result is preserved even when coplanar dislocation reactions are involved since a triple node with 120° emerging lines with edge character can actually be created.

For dislocations whose glide plane intersects the pore, we have shown the importance of the strong elastic anisotropy on the CMSX-4 superalloy at high homologous temperature on the dislocation behavior. More precisely, the anisotropy is at the origin of the formation of stable dislocations loop emerging from the pore. These stable loops may favor the contribution of pore closure induced by the formation of prismatic loops resulting from cross-slip events of the screw parts of the loop.

Then, the arrangement of dislocations constituting a tilt LAB and localized in the vicinity of a pore is also characterized. Finally, scenarios of dislocation induced pore closure are proposed based on the obtained results and the available literature. Further investigations are required to clarify the importance of cross-slip and dislocation climb using the maturing of continuous or discrete mesoscopic models of dislocation dynamics. Dislocation density based models may also constitute relevant alternatives [43].

An interesting perspective of this work may be envisaged from an experimental point of view. By considering a model HIPed FCC γ-alloy (without γ' precipitates perturbating any characterization), one could envisage to realize post-mortem FIB specimens with selected crystallographic orientations and observe dislocations arrangement in the vicinity of a pore; we could then be able to verify whether a higher density of dislocation is identified along the four octahedral directions, as found in our simulations, and also provide new insights on the competitive mechanisms involved during HIP and subject to interplay with gliding dislocations.

Acknowledgments and founding

We gratefully acknowledge the German Scientific Research Foundation DFG (grants EP 136/1-1 and FE 933/2-1) and the financial support from the French National Research Agency ANR (grants ANR15-MERA-0003-03).

Data availability

The raw/processed data required to reproduce these findings can be provided by the authors on request.

Appendix A. Phase-field model of dislocations

In the PFMD, the material is described with the help of continuous fields defined at each position $\overrightarrow{r}$ that reflects both its constitutive elastic behavior and the presence of dislocations. The relevant fields are strains ε_{ij} for the elastic behavior and phase-fields η_s for dislocations. In practice, η_s reflects the amplitude of glide for each of the $s = 1$ to 12 FCC slip-systems related to each of the dislocation-induced sheared phases. These fields are involved in the definition of a free energy $\mathcal{F}$ that can be written as an integral over the volume V:

$$\mathcal{F} = \int_V f_{el}\left(\{\varepsilon_{ij}\},\{\eta_s\}\right) + f_{cryst}\left(\{\eta_s\}\right) + f_{grad}\left(\{\eta_s\}\right)\ \mathrm{d}V. \tag{A.1}$$

In this formula, f_{el} is the elastic energy density which is written in the small deformation framework:

$$f_{el} = \frac{1}{2} C_{ijkl}\left(\varepsilon_{ij} - \varepsilon^0_{ij}\right)\left(\varepsilon_{kl} - \varepsilon^0_{kl}\right), \tag{A.2}$$

where C_{ijkl} are the elastic coefficients whose value can vary in space. In a cubic crystal, use is made of the Voigt notation to define the three independent elastic coefficients C_{11}, C_{12} and C_{44}. The bulk modulus K and shear modulus C' are alternative elastic coefficients defined by $K = (C_{11} + 2C_{12})/3$ and $C' = (C_{11} - C_{12})/2$. ε_{ij} is the total strain:

$$\varepsilon_{ij} = \frac{1}{2}\left(\frac{\partial u_i}{\partial X_j} + \frac{\partial u_j}{\partial X_i}\right), \tag{A.3}$$

and u_i are the displacement component (X_i are the coordinates of a point taken in the undeformed reference state). ε^0_{ij} is the eigenstrain related to dislocations given by:

$$\varepsilon^0_{ij} = \sum_{s=1}^{12} \frac{b_{i/s}\ n_{j/s} + b_{j/s}\ n_{i/s}}{2h} g\left(\eta_s\right), \tag{A.4}$$

with an interpolating function taken from [44]:

$$g\left(\eta_s\right) = \eta_s - \frac{\sin(2\pi\eta_s)}{2\pi}, \tag{A.5}$$

where, for each slip-system s, b_i is a Burgers vector component, n_i is a component of the normal unit vector of the corresponding slip-plane and h the $\{111\}$ FCC interlayer spacing. For a FCC material, we consider the 12 octahedral slip-systems $1/2\langle 110\rangle\{111\}$ with the nomenclature of Tab. A.2.

$\overrightarrow{n}_s$	$\overrightarrow{b}_s$		
$\overrightarrow{n}_{1,2,3} = [1\bar{1}1]/\sqrt{3}$	$\overrightarrow{b}_1 = a_0/2[110]$	$\overrightarrow{b}_2 = a_0/2[\bar{1}01]$	$\overrightarrow{b}_3 = a_0/2[0\bar{1}\bar{1}]$
$\overrightarrow{n}_{4,5,6} = [\bar{1}11]/\sqrt{3}$	$\overrightarrow{b}_4 = a_0/2[100]$	$\overrightarrow{b}_5 = a_0/2[\bar{1}\bar{1}0]$	$\overrightarrow{b}_6 = a_0/2[01\bar{1}]$
$\overrightarrow{n}_{7,8,9} = [111]/\sqrt{3}$	$\overrightarrow{b}_7 = a_0/2[1\bar{1}0]$	$\overrightarrow{b}_8 = a_0/2[\bar{1}01]$	$\overrightarrow{b}_9 = a_0/2[01\bar{1}]$
$\overrightarrow{n}_{10,11,12} = [11\bar{1}]/\sqrt{3}$	$\overrightarrow{b}_{10} = a_0/2[101]$	$\overrightarrow{b}_{11} = a_0/2[\bar{1}10]$	$\overrightarrow{b}_{12} = a_0/2[0\bar{1}\bar{1}]$

Table A.2: Normal unit vectors $\overrightarrow{n}_s$ and Burgers vectors $\overrightarrow{b}_s$ related to the 12 octahedral slip-systems $1/2\langle 110\rangle\{111\}$. a_0 is the FCC lattice parameter.

In Eq. (A.1), f_{cryst} is the Landau bulk energy density related to the dislocation-induced sheared phases. In the present context, this term is related to the symmetry of the $\{111\}$ generalized stacking fault energy in relation to the FCC crystallography. For reasons explained in [45], this contribution is

taken to be:

$$\begin{aligned} f_{cryst} &= 2A\{4 - \cos[\pi(\eta_1 - \eta_2)]\cos[\pi(\eta_2 - \eta_3)] \\ &\quad \cos[\pi(\eta_3 - \eta_1)] \\ &\quad - \cos[\pi(\eta_4 - \eta_5)]\cos[\pi(\eta_5 - \eta_6)] \\ &\quad \cos[\pi(\eta_6 - \eta_4)] \\ &\quad - \cos[\pi(\eta_7 - \eta_8)]\cos[\pi(\eta_8 - \eta_9)] \\ &\quad \cos[\pi(\eta_9 - \eta_7)] \\ &\quad - \cos[\pi(\eta_{10} - \eta_{11})]\cos[\pi(\eta_{11} - \eta_{12})] \\ &\quad \cos[\pi(\eta_{12} - \eta_{10})]\}, \end{aligned} \tag{A.6}$$

where A is a parameter of the model.

The last term of Eq. (A.1) is the Ginzburg penalty core energy density taken from [45]:

$$f_{grad} = \frac{B}{2}\sum_{s,s'=1}^{12} \frac{\overrightarrow{b}_s \cdot \overrightarrow{b}_{s'}}{b^2}\left(\overrightarrow{n}_s \times \overrightarrow{\nabla}\eta_s\right)\cdot\left(\overrightarrow{n}_{s'} \times \overrightarrow{\nabla}\eta_{s'}\right), \tag{A.7}$$

where B is another parameter of the model.

It is shown in [12] that A and B are related to the core energy (per unit length) W_{core} and the core size ξ of a dislocation:

$$W_{core} = \frac{4d}{\pi\sqrt{3}}\sqrt{AB} \quad \text{and} \quad \xi = \frac{1}{2\pi}\sqrt{\frac{B}{A}}, \tag{A.8}$$

where d is the numerical grid spacing. The first quantity is chosen with the physical constraint: $W_{core} \approx 0.1\mu b^2$ (μ is the shear modulus and b the Burgers vector's norm). The second is chosen with the numerical constraint: $\xi \approx 0.5d$.

Dislocation mobility is controlled by a relaxation equation on phase-fields η_s usually called the Allen-Cahn equation:

$$\frac{\partial \eta_s}{\partial t} = -L\frac{\delta \mathcal{F}}{\delta \eta_s}, \tag{A.9}$$

where L is a mobility coefficient. Elastic fields are dissipatively relaxed at each time step of the dislocation mobility so their movement is assumed to be quasi-static.

It is shown in [12] that L is related to the frictional coefficient B_{fr} involved in the classical relationship $B_{fr}v = b\tau$ linking the dislocation velocity v to the resolved shear stress τ [19]:

$$L = \frac{2h}{B_{fr}\pi^2\xi}. \tag{A.10}$$

In pure metals, this linear relationship is experimentally related to phonon drag mechanisms and B_{fr} is nothing but the phonon drag coefficient. This former relationship enables us to define the characteristic time-scale of our simulations:

$$t_0 = \frac{\pi^2\sqrt{3}}{4}\left(\frac{d}{a_0}\right)^2\frac{B_{fr}}{K}, \tag{A.11}$$

where K is the bulk modulus. In [12], we used experimental data in a Re containing Ni-base superalloy at $T = 350$ °C to estimate $B_{fr} \approx 10^4$ Pa.s. By considering $d/a_0 = 648$ and $K = 165$ GPa, one gets $t_0 \approx 0.1$ s. That said, there is no similar experimental data on the dislocation velocities in CMSX-4 at high homologous temperature that could be used to estimate a value of B_{fr} relevant in HIP conditions.

Numerically, the fields are discretized on a FCC finite difference grid also exposed in [12] that allows us to consider a heterogeneous material in which a circular cavity of zero stiffness can be sharply introduced without generating any numerical artifacts. As the mechanical equilibrium is reached, the stress field generated by a pore under external pressure and that originated from dislocations are fully computed whether the material is elastically isotropic or anisotropic. Hence, the coupling of fields within the variational formalism naturally accounts for all the elastic interactions between the dislocations themselves and with the free surface of a pore.

References

[1] K. Harris, G. Erickson, S. Sikkenga, W. Brentnall, J. Aurrecoechea, K. Kubarych, Development of two rhenium-containing superalloys for single-crystal blade and directionally solidified vane applications in advanced turbine engines, Journal of materials engineering and performance 2 (4) (1993) 481–487.

[2] K. P. Fullagar, R. W. Broomfield, M. Hulands, K. Harris, G. L. Erickson, S. L. Sikkenga, Aero engine test experience with cmsx-4® alloy single-crystal turbine blades, Journal of Engineering for Gas Turbines and Power 118 (2) (1996) 380–388.

[3] T. Link, S. Zabler, A. Epishin, A. Haibel, M. Bansal, X. Thibault, Synchrotron tomography of porosity in single-crystal nickel-base superalloys, Materials Science and Engineering: A 425 (1-2) (2006) 47–54.

[4] B. S. Bokstein, A. Epishin, V. Esin, M. Mendelev, A. Rodin, S. Zhevnenko, Cross diffusion-stresses effects, in: Defect and Diffusion Forum, Vol. 264, Trans Tech Publ, 2007, pp. 79–89.

[5] U. Brückner, A. Epishin, T. Link, Local x-ray diffraction analysis of the structure of dendrites in single-crystal nickel-base superalloys, Acta materialia 45 (12) (1997) 5223–5231.

[6] A. Epishin, T. Link, U. Bruckner, P. Portella, Investigation of porosity in single-crystal nickel-base superalloys, in: Proceedings of the 7th Conference on Materials for Advanced Power Engineering, Liege, 2002, pp. 217–226.

[7] A. Epishin, T. Link, I. L. Svetlov, G. Nolze, R. S. Neumann, H. Lucas, Mechanism of porosity growth during homogenisation in single crystal nickel-based superalloys, International Journal of Materials Research 104 (8) (2013) 776–782.

[8] I. M. Razumovskii, A. A. Tikhonov, S. Marinin, A. Logunov, A. Beresnev, Hot isostatic pressing improves the quality of the blades from nickel base superalloys for turbine engines, in: Advanced Materials Research, Vol. 278, Trans Tech Publ, 2011, pp. 295–300.

[9] A. Epishin, B. Fedelich, G. Nolze, S. Schriever, T. Feldmann, M. F. Ijaz, B. Viguier, D. Poquillon, Y. Le Bouar, A. Ruffini, et al., Creep of single crystals of nickel-based superalloys at ultra-high homologous temperature, Metallurgical and Materials Transactions A 49 (9) (2018) 3973–3987.

[10] A. I. Epishin, B. S. Bokstein, I. L. Svetlov, B. Fedelich, T. Feldmann, Y. Le Bouar, A. Ruffini, A. Finel, B. Viguier, D. Poquillon, A vacancy model of pore annihilation during hot isostatic pressing of single crystals of nickel-base superalloys, Inorganic Materials: Applied Research 9 (1) (2018) 57–65.

[11] A. Epishin, B. Fedelich, T. Link, T. Feldmann, I. L. Svetlov, Pore annihilation in a single-crystal nickel-base superalloy during hot isostatic pressing: Experiment and modelling, Materials Science and Engineering: A 586 (2013) 342–349.

[12] A. Ruffini, Y. Le Bouar, A. Finel, Three-dimensional phase-field model of dislocations for a heterogeneous face-centered cubic crystal, Journal of the Mechanics and Physics of Solids 105 (2017) 95–115.

[13] G. Lamé, Leçons sur la théorie mathématique de l'élasticité des corps solides, bachelier Edition, 1852.

[14] L. Landau, E. M. Lifshits, Theory of elasticity, elsevier science Edition, 1986.

[15] J. Hirth, J. Lothe, Theory of dislocations, john wiley and sons Edition, 1982.

[16] W. T. Read, W. Shockley, Dislocation models of crystal grain boundaries, Physical review 78 (3) (1950) 275.

[17] A. Epishin, B. Fedelich, M. Finn, G. Künecke, B. Rehmer, G. Nolze, C. Leistner, N. Petrushin, I. Svetlov, Investigation of elastic properties of the single-crystal nickel-base superalloy cmsx-4 in the temperature interval between room temperature and 1300° c, Crystals 11 (2) (2021) 152.

[18] D. Bacon, D. Barnett, R. O. Scattergood, Anisotropic continuum theory of lattice defects, Progress in Materials Science 23 (1980) 51–262.

[19] L. Kubin, Dislocations, mesoscale simulations and plastic flow, Vol. 5, Oxford University Press, 2013.

[20] F. R. N. Nabarro, Mathematical theory of stationary dislocations, Advances in Physics 1 (3) (1952) 269–394.

[21] S. Gavazza, D. Barnett, The self-force on a planar dislocation loop in an anisotropic linear-elastic medium, Journal of the Mechanics and Physics of Solids 24 (4) (1976) 171–185.

[22] V. Lubarda, M. Schneider, D. Kalantar, B. Remington, M. Meyers, Void growth by dislocation emission, Acta Materialia 52 (6) (2004) 1397–1408.

[23] J. Marian, J. Knap, M. Ortiz, Nanovoid cavitation by dislocation emission in aluminum, Physical review letters 93 (16) (2004) 165503.

[24] S. Traiviratana, E. M. Bringa, D. J. Benson, M. A. Meyers, Void growth in metals: atomistic calculations, Acta Materialia 56 (15) (2008) 3874–3886.

[25] E. M. Bringa, S. Traiviratana, M. A. Meyers, Void initiation in fcc metals: effect of loading orientation and nanocrystalline effects, Acta Materialia 58 (13) (2010) 4458–4477.

[26] C. Mi, D. A. Buttry, P. Sharma, D. A. Kouris, Atomistic insights into dislocation-based mechanisms of void growth and coalescence, Journal of the Mechanics and Physics of Solids 59 (9) (2011) 1858–1871.

[27] Y. Cui, Z. Chen, Material transport via the emission of shear loops during void growth: A molecular dynamics study, Journal of Applied Physics 119 (22) (2016) 225102.

[28] L. Nguyen, D. Warner, Improbability of void growth in aluminum via dislocation nucleation under typical laboratory conditions, Physical review letters 108 (3) (2012) 035501.

[29] L. Zhao, Y. Liu, Investigation on void growth and coalescence in single crystal copper under high-strain-rate tensile loading by atomistic simulation, Mechanics of Materials 151 (2020) 103615.

[30] R. B. Sills, B. Boyce, Void growth by dislocation adsorption, Materials Research Letters 8 (3) (2020) 103–109.

[31] L. B. Munday, J. C. Crone, J. Knap, The role of free surfaces on the formation of prismatic dislocation loops, Scripta Materialia 103 (2015) 65–68.

[32] L. B. Munday, J. C. Crone, J. Knap, Prismatic and helical dislocation loop generation from defects, Acta Materialia 103 (2016) 217–228.

[33] M. Huang, Z. Li, C. Wang, Discrete dislocation dynamics modelling of microvoid growth and its intrinsic mechanism in single crystals, Acta Materialia 55 (4) (2007) 1387–1396.

[34] H.-J. Chang, J. Segurado, J. LLorca, Three-dimensional dislocation dynamics analysis of size effects on void growth, Scripta Materialia 95 (2015) 11–14.

[35] V. V. Bulatov, W. G. Wolfer, M. Kumar, Shear impossibility: Comments on "void growth by dislocation emission" and "void growth in metals: Atomistic calculations", Scripta Materialia 63 (1) (2010) 144–147.

[36] P.-A. Geslin, B. Appolaire, A. Finel, Investigation of coherency loss by prismatic punching with a nonlinear elastic model, Acta materialia 71 (2014) 80–88.

[37] M. Ashby, L. Johnson, On the generation of dislocations at misfitting particles in a ductile matrix, Philosophical Magazine 20 (167) (1969) 1009–1022.

[38] V. Krasnikov, A. Mayer, Plasticity driven growth of nanovoids and strength of aluminum at high rate tension: Molecular dynamics simulations and continuum modeling, International Journal of Plasticity 74 (2015) 75–91.

[39] Y. Zhang, S. Jiang, X. Zhu, Y. Zhao, Influence of void density on dislocation mechanisms of void shrinkage in nickel single crystal based on molecular dynamics simulation, Physica E: Low-dimensional Systems and Nanostructures 90 (2017) 90–97.

[40] Y.-L. Guan, J.-L. Shao, W. Song, Molecular dynamics study on nanoscale void collapse in single crystal aluminum under 1d and 3d compressions, Computational Materials Science 161 (2019) 385–393.

[41] P.-A. Geslin, B. Appolaire, A. Finel, A phase field model for dislocation climb, Applied Physics Letters 104 (1) (2014) 011903–011903–4.

[42] A. Epishin, Private communication (2016).

[43] P.-L. Valdenaire, Y. Le Bouar, B. Appolaire, A. Finel, Density-based crystal plasticity: From the discrete to the continuum, Physical Review B 93 (21) (2016) 214111.

[44] S. Hu, Y. Li, Y. Zheng, L. Chen, Effect of solutes on dislocation motion —a phase-field simulation, Owen Richmond Memorial Special Issue 20 (3) (2004) 403–425.

[45] C. Shen, Y. Wang, Phase field model of dislocation networks, Acta materialia 51 (9) (2003) 2595–2610.

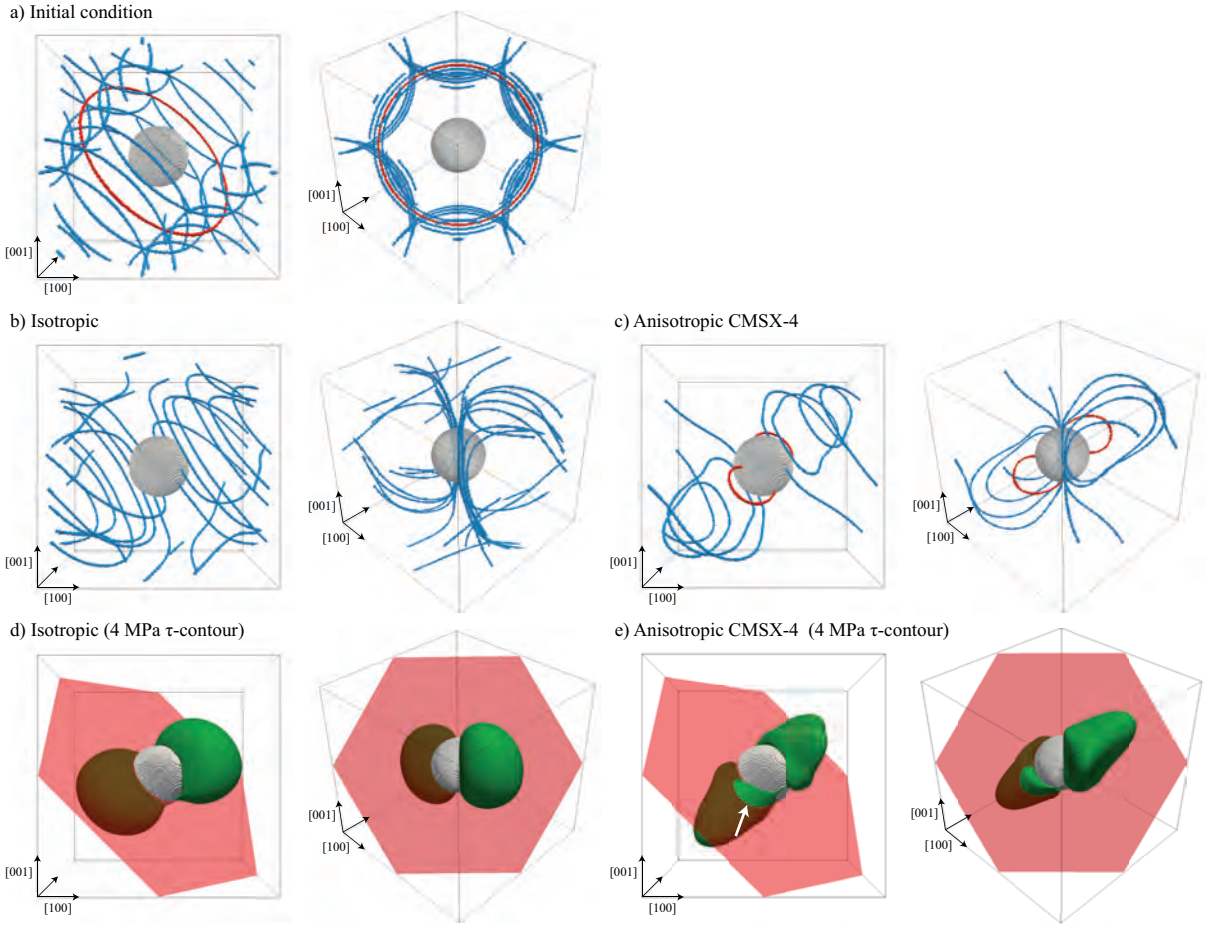

Figure 6: Dislocation loops from the slip-system $s = 1$, initially introduced in five slip-planes of type $(1\bar{1}1)$. The loop introduced in the equatorial slip-plane is in red while the other are in blue (a). Final configuration of the loops in the model isotropic crystal (b) and in the anisotropic CMSX-4 (c). These configurations are placed in comparison to the 4 MPa τ-contours related to the isotropic (d) and anisotropic CMSX-4 crystals (e), respectively. The τ-contours enclose a green region where $\tau > 4$ MPa. The external region is related to $\tau < 4$ MPa. The translucent red plane is the $(1\bar{1}1)$ plane intersecting pore equator. (See colors on-line)

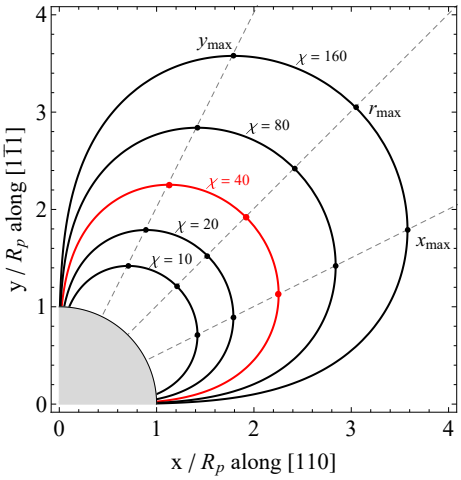

Figure 7: Equilibrium position, y_{max}, r_{max} and x_{max} given by Eqs. (9 – 11) as a function of χ in the positive quarter of $(0; \overrightarrow{e_x}, \overrightarrow{e_y})$ basis exposed in Fig. 5b with the pore (in gray). The case $\chi = 45.41 \approx 40$ related to the simulations is in red. (See colors on-line)

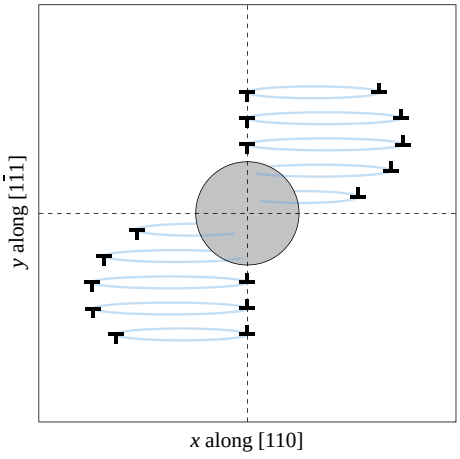

Figure 8: Final expected equilibrium arrangement of dislocation loops around the pore (in gray) by considering slip-system $\overrightarrow{b} = a_0/2[110]$ and $\overrightarrow{n} = [1\bar{1}1]/\sqrt{3}$ in the $(0; \overrightarrow{e_x}, \overrightarrow{e_y})$ basis defined by $\overrightarrow{e_x} = \overrightarrow{b}/b$ and $\overrightarrow{e_y} = \overrightarrow{n}$.

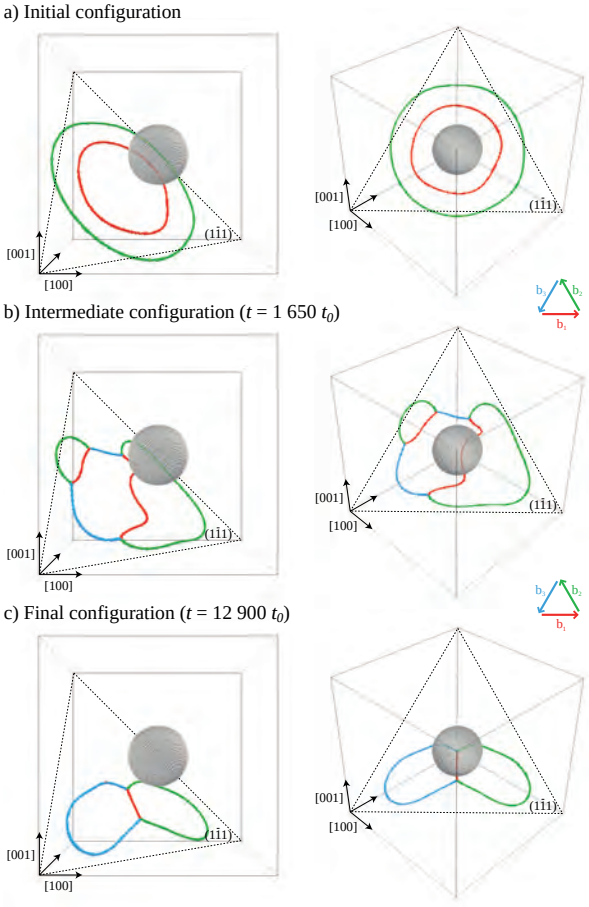

Figure 9: Dislocation loops from the slip-system $s = 1$ (in red) and $s = 2$ (in green), initially introduced in a plane $(1\bar{1}1)$ that does not intersect the pore (a). Intermediate configuration in the elastically anisotropic CMSX-4 showing the formation of dislocation segments from slip-system $s = 3$ (in blue) that result from the coplanar reaction of the first two (b). Final configuration of the loops (c). (See colors on-line)

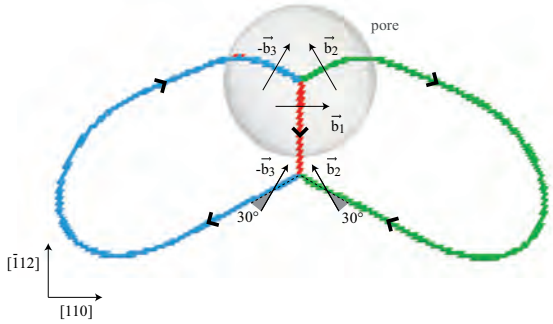

Figure 10: Final configuration of two coplanar dislocation loops originated from two different slip-systems in the anisotropic CMSX-4. (See colors on-line)

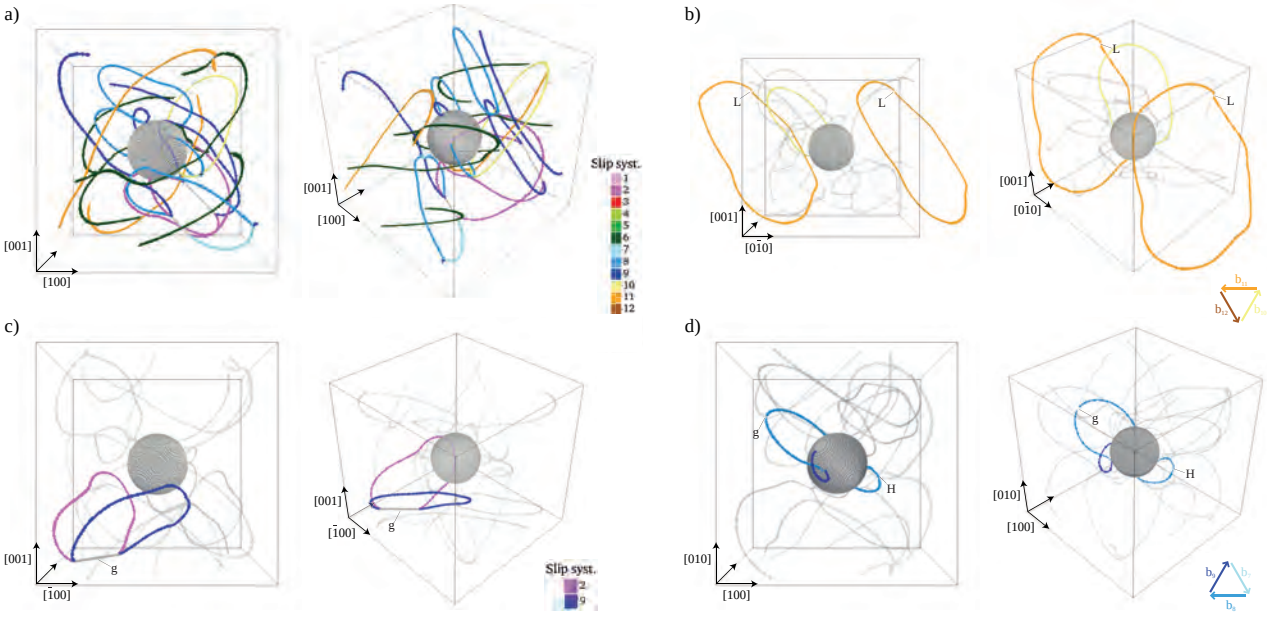

Figure 11: (a) Final configuration resulting from the evolution of twenty-four initial circular dislocation loops of random radii and positions, arbitrary chosen from every slip-systems. Dislocations from slip-systems 1 to 3 are colorized in a hue of red, those from 4 to 6 in a hue of green, those from 7 to 9 in a hue of blue and those from 10 to 12 in a hue of yellow. Glissile junctions [g], Lomer [L] and Hirth locks [H] are directly indicated with the corresponding letters. Figs. (b), (c) and (d) emphasize specific loops commented in the text at points (i), (ii) and (iii) respectively. (See colors on-line)

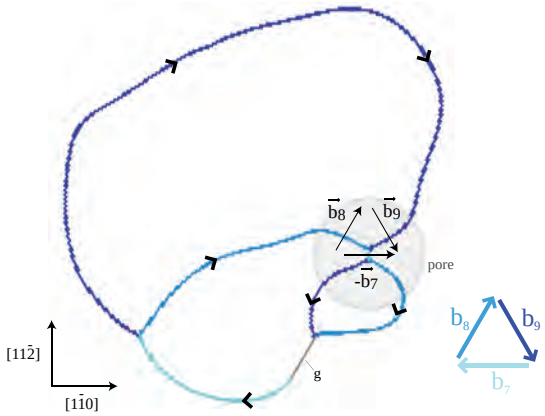

Figure 12: Final configuration of loops from slip-systems 7 to 9 such as they can be found in Fig. 11a and resulting from coplanar dislocation reactions. Loops are in hue of blue while the glissile junction [g] resulting from loops ss7 and ss2 (not shown in the figure) is in gray. (See colors on-line)

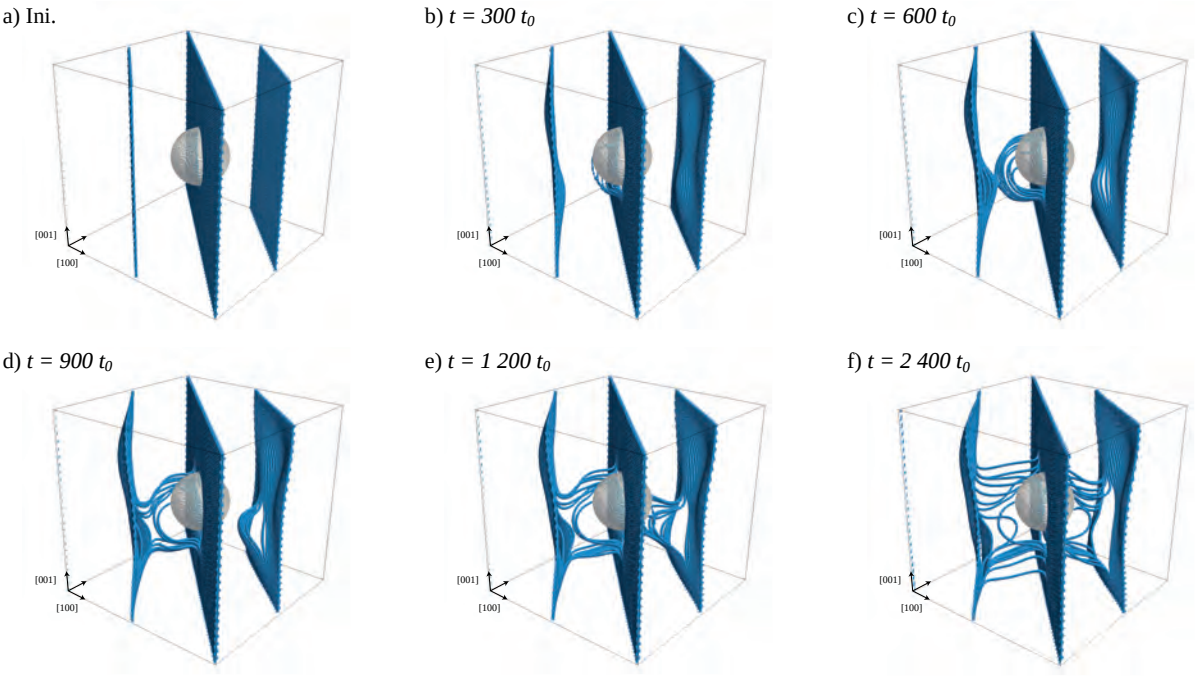

Figure 13: Pore (in gray) embedded in a tilt LAB made with straight edge dislocations (in blue) from the first slip-system (a). Destabilization of the LAB under the stress field generated by the pore as time t increases (b – f). The time is given in unit t_0 given Eq. (A.11). (See colors on-line)

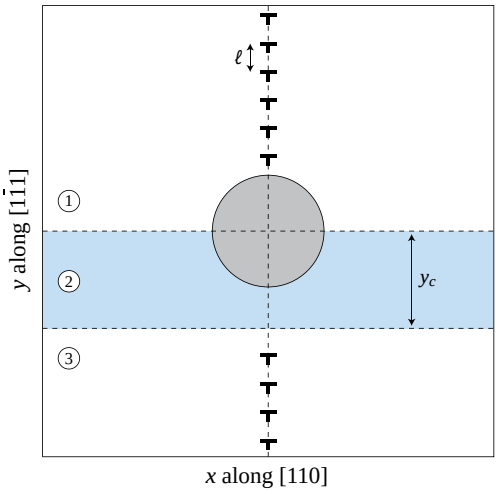

Figure 14: Final expected configuration of a pore interacting with a tilt LAB built with stacking edge dislocations belonging to slip-system $\overrightarrow{b}_1 = a_0/2[110]$ and $\overrightarrow{n} = [1\bar{1}1]/\sqrt{3}$ in the $(0; \overrightarrow{e_x}, \overrightarrow{e_y})$ basis defined by $\overrightarrow{e_x} = \overrightarrow{b}/b$ and $\overrightarrow{e_y} = \overrightarrow{n}$. Region ① corresponds to the region where dislocations are stabilized by the the stress field generated by both pore and LAB. In region ②, dislocations are destabilized by the stress field generated by the pore. In region ③, the destabilization stress field induced by the pore is compensated by that of the LAB.

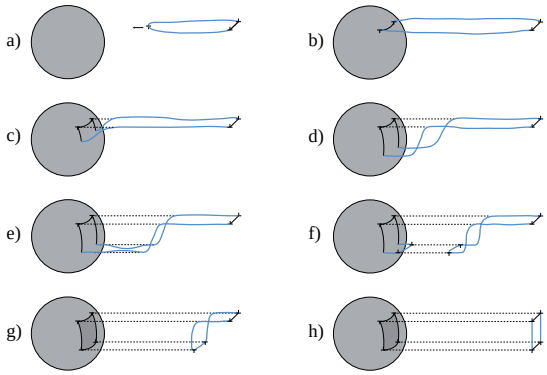

Figure 15: Scenario of pore closure involving cross-slip generated prismatic loop. The starting point would be a preexisting shear dislocation loop that would anchor to the pore. Screw parts of the shear loop would cross-slip on the pore surface. This would allow a prismatic loop to be formed, placing the dislocation segments further away from the surface where the image force would notably be weaker. It would then allow for the "plane from pore" edge part of the loop to be pushed forward and a prismatic plane to be introduced, whether by a line-tension induced detaching process or another cross-slip mechanism.

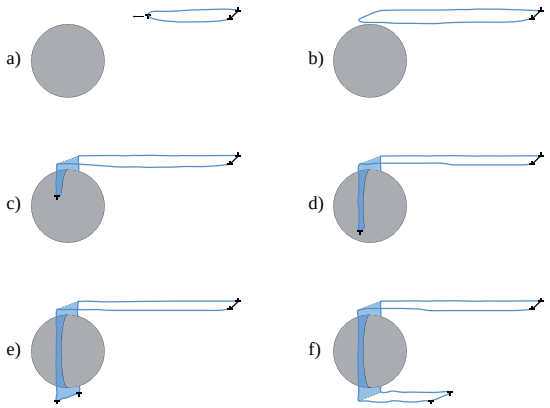

Figure 16: Glide – Climb scenario inducing pore closure [42]. The starting point would be a preexisting shear dislocation whose "plane to pore" edge part would be placed just above the pore surface. This "plane to pore" edge part would then climb through the absorption of vacancies in a (110) crystallographic plane (in blue), allowing the removal of one atomic plane. Under the equatorial plane of the pore, we can speculate that the dislocation line would continue its movement. By becoming a "plane from pore" edge repulsive part, it may finally be pushed forward by glide. (See colors on-line)